Proceedings of the Seventh International Conference on
Railway Technology: Research, Development and Maintenance
Edited by: J. Pombo
Civil-Comp Conferences, Volume 15, Paper 18.10
Civil-Comp Press, Edinburgh, United Kingdom, 2026
ISSN: 2753-3239, doi: 10.4203/ccc.15.18.10

Macro- and Microscopic Dynamic Responses of Coupled Train-Ballasted Track-Subgrade System via Hybrid MBD-DEM FDM Method

Y. Chen and Y. Xiao

**Central South University,
China**

Abstract

With the growing complexity of high-speed railway operations, the train-ballasted track-subgrade system is increasingly subjected to intensified dynamic loads and operational demands, posing significant challenges to structural integrity and maintenance strategies. However, most existing numerical models treat the train, track, ballast, and subgrade as decoupled subsystems, thereby failing to capture the essential dynamic interactions within this integrated system. To address this limitation, this study proposes and develops a coupled multi-scale dynamic simulation framework that integrates a Multi-Body Dynamics (MBD) model for the train, a Discrete Element Method (DEM) model for ballast particles, and a Finite Difference Method (FDM) model for the continuous subgrade. This framework enables a comprehensive investigation of both macro- and micro-scale dynamic responses under varying train speeds ranging from 250 to 350 km/h. The results show that the vertical acceleration of the train body increases by 25% as speed rises, while lateral acceleration and wheel-rail contact forces increase by 85.9% and 54.7%, respectively. Speed-dependent precursor displacements are observed in the rail and sleeper, and ballast deformation at 350 km/h increases by 144% compared to that at 250 km/h. At the granular scale, the proportion of sliding contacts among ballast particles increases by 64% when train speed exceeds 325 km/h, the force chain network becomes more dispersed, and up to 73% of the sleeper base load is carried by force chains. These findings suggest that 325 km/h may serve as a critical threshold for ballast maintenance, indicating the need for enhanced monitoring and more frequent ballast replenishment in key zones. The multi-scale modeling strategy proposed herein offers

novel theoretical insights and methodological guidance for dynamic analysis and intelligent maintenance of high-speed railway infrastructure.

Keywords: train-ballasted track-subgrade system, multi-body dynamics, discrete element method, finite difference method, macro-microscale dynamic response, coupled modeling

1 Introduction

Ballasted tracks remain essential in some high-speed railways for their cost-effectiveness and easy maintenance, but repetitive train loads lead to ballast degradation, reduced stiffness, and failures such as mud pumping and loss, threatening stability. Therefore, it is imperative to develop a high-fidelity coupled train-track-subgrade system model to elucidate the underlying degradation mechanisms and inform the design and maintenance strategies of railway infrastructure. Existing studies employing CAE software [1] or self-programmed codes often simplify the train subsystem into excitation functions [2] or rely on limited software coupling [3]. Although self-developed approaches have introduced nonlinear wheel-rail contact [4], dynamic substructuring [5], and track deterioration effects [6], the ballast layer is still commonly treated as a continuum or a mass-spring-damper system. Such simplifications overlook critical mesoscopic features, including particle geometry, random contact interactions, and micromechanical behaviors. By contrast, the DEM enables particle-scale analysis. Studies by McDowell [7], Indraratna et al. [8], and Tutumluer [9] have revealed ballast kinematics and force chain evolution under cyclic loading. Recent efforts to couple MBD with DEM [10] have advanced vehicle-ballast interaction modeling but are typically restricted to two dimensions or simplified load inputs. In summary, most existing studies have yet to realize fully coupled, three-dimensional, real-time simulations that integrate the train, track, and granular ballast subsystems. To bridge this gap, the present study proposes a comprehensive coupled dynamic simulation framework that integrates a MBD model for the vehicle subsystem, a DEM model for the granular ballast layer, and a FDM model for the continuous subgrade. Based on this integrated approach, a systematic analysis of both macro- and micro-scale dynamic responses is conducted under varying operating speeds (250~350 km/h). The findings provide novel theoretical insights and robust methodological support for the dynamic assessment and intelligent maintenance of high-speed railway infrastructure.

2 Methods and model validation

2.1. Hybrid MBD-DEM-FDM Modeling of Train-ballasted track-subgrade system

This study establishes a multi-scale coupled framework for simulating the high-speed train-ballasted track-subgrade system by integrating MBD-DEM-FDM, see Figure 1. The train subsystem is modeled in MBD with 38 degrees of freedom, employing Hertzian contact for normal forcesand Kalker’s linear creep theory for tangential forces, while track irregularities are introduced as excitations based on established spectral methods [11]. The ballast bed is simulated in PFC3D using DEM, where aggregates are idealized as spheres governed by the Rolling Resistance Linear Model [12], and staged compaction replicates tamping operations [13]. Sleepers and the subgrade are represented via FDM, with refined discretization according to wavelength criteria [14]. As illustrated in Fig. 1, the model has a total length of 132 m and includes 220 sleepers (50+20+150). The effective running length of the train within the model is 47.25 m. In the longitudinal direction, the model domain is divided into a foundation transition zone and a core coupling zone. Within the foundation transition zones, the rail and sleeper models are represented by spring-damper elements combined with viscoelastic boundaries. The left transition zone (50 sleepers) ensures that the train gradually evolves from a static state to steady-state operation, while the right transition zone (150 sleepers) provides sufficient space for the attenuation of dynamic waves. A buffering segment consisting of 100 sleepers is introduced to mitigate the influence of wave reflections from the computational boundaries on the responses of the core coupling region. Thereby, it achieves a balance among computational accuracy, physical realism, and computational efficiency. The core coupling zone (20 sleepers) incorporates rail, sleepers, underlying ballast, and a subgrade mass block model constructed using spring-damper elements and viscoelastic boundaries. At the 10th sleeper, coupling conditions among the MBD-DEM-FEM modules are implemented to capture representative macro- and micro-scale responses of the ballast under train-induced dynamic loading.

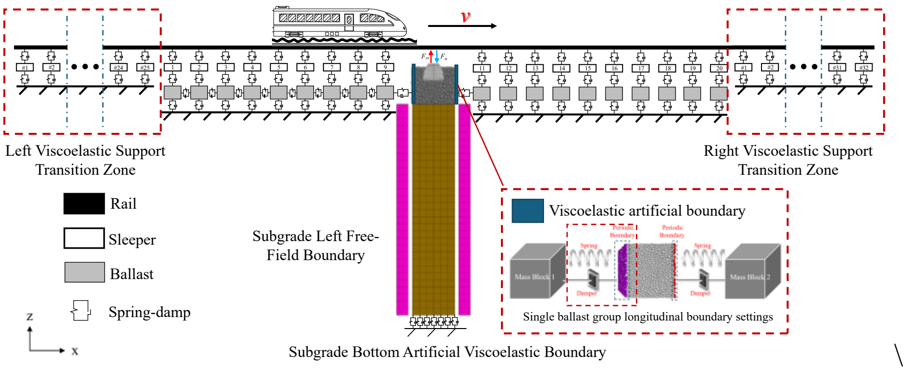

Fig. 1. Overall coupling model in the longitudinal direction.

The specific coupling scheme is illustrated in Fig. 2, where real-time bidirectional MBD-DEM-FEM coupling is implemented through the Service-link interface using Python. The Service-link interface consists of Rail-Fastener-Sleeper Coupling Module and the Ballast Particle-Mass Block Spring-Damper Coupling Module. Within the Rail-Fastener-Sleeper Coupling Module, the MBD module outputs the fastener force obtained from the previous time step and applies it to the FDM sleeper model. The sleeper then transfers the interaction forces to both the DEM ballast module and the FDM subgrade model through the Socket I/O interface provided by Itasca [15]. After completing the calculation for one time step, the reaction forces are returned to the MBD module, thereby achieving bidirectional coupling [16]. It should be noted that the time step used in the simulation is 0.001 s, determined based on the

Wilson-θ method time integration scheme [17]. Meanwhile, within the Ballast Particle-Mass Block Spring-Damper Coupling Module, the spring-damper forces of the ballast mass block elements calculated in the MBD module at the previous time step are equivalently discretized and applied to the boundary particles of the DEM ballast assembly. After the DEM calculation advances by one time step, the resultant spring-damper forces are recalculated based on the centroid displacement, velocity, and acceleration of the particle assembly and subsequently transmitted back to the MBD module [18].

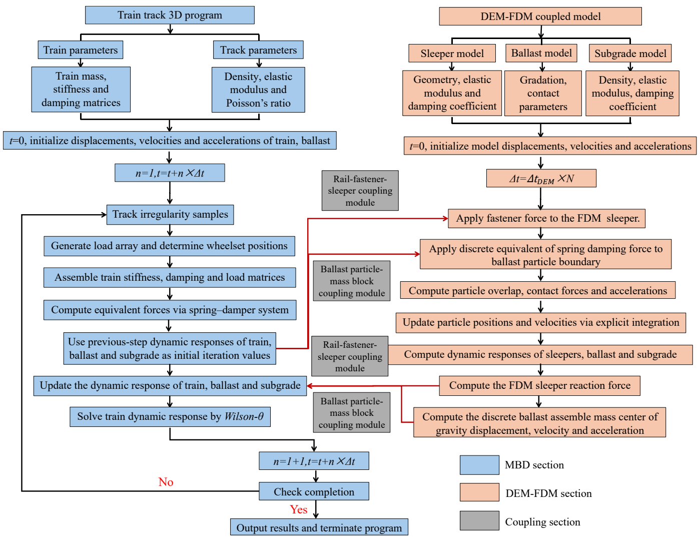

Fig. 2. Overall coupling model in the longitudinal direction.

2.2 Rail-Fastener-Sleeper Coupling Module

In the MBD module, the fasteners are modeled using a spring-damper system. To equivalently simulate the mechanical behavior of the fasteners in the DEM module, the equivalent spring-damper forces are calculated based on the relative displacement and velocity between the rail and the sleeper, and these forces are applied at the bonding interface between the sleeper and the fastener. The equivalent forces at the fastener locations in the 3D directions are computed and applied to the corresponding coupling positions on the FDM sleepers. Subsequently, after a time step calculation, the displacements and velocities of the sleepers in the 3D directions are extracted, and the reaction forces are calculated using the following equations:

$$\begin{cases} F_{x1} = k_x(x_{rx1} - x_{sx}) + C_x(v_{rx1} - v_{sx}) \\ F_{y1} = k_y(x_{ry1} - x_{sy}) + C_y(v_{ry1} - v_{sy}) \\ F_{z1} = k_z(x_{rz1} - x_{sz}) + C_z(v_{rz1} - v_{sz}) \end{cases} \tag{1}$$

$$\begin{cases} F_{x2} = k_x(x_{rx2} - x_{sx}) + C_x(v_{rx2} - v_{sx}) \\ F_{y2} = k_y(x_{ry2} - x_{sy}) + C_y(v_{ry2} - v_{sy}) \\ F_{z2} = k_z(x_{rz2} - x_{sz}) + C_z(v_{rz2} - v_{sz}) \end{cases} \tag{2}$$

where F_{x1}, F_{y1}, F_{z1} and F_{x2}, F_{y2}, F_{z2} denote the reaction forces returned to the fasteners on the left and right sleepers in the respective directions, respectively; k_x, k_y, k_z are the spring stiffness coefficients of the fastener, respectively; c_x, c_y, c_z are the damping coefficients, respectively; x_{rx1}, x_{ry1}, x_{rz1} and x_{rx2}, x_{ry2}, x_{rz2} are the displacements of the left and right rails, respectively; v_{rx1}, v_{ry1}, v_{rz1} and v_{rx2}, v_{ry2}, v_{rz2} are the corresponding rail velocities, respectively; and x_{sx}, x_{sy}, x_{sz} and v_{sx}, v_{sy}, v_{sz} are the sleeper displacements and velocities, respectively.

Based on force-displacement coordination and Newton's third law, a method is proposed to account for the coordination between force and deformation at fastener locations in 3D space. The fastener force from the previous time step is taken as the initial iterative force and transmitted through the fasteners to the corresponding positions at the top of the FDM sleepers model. The dynamic responses of the rail and sleeper are then updated, and the reaction forces of the ballast-subgrade system are calculated. If the difference between the applied force and the reaction force exceeds the set threshold (100 N), the simulation proceeds to the next time step for dynamic analysis. If this condition is not met, the input force needs to be corrected, and the specific flow chart is shown in Fig. 3. The correction formula is as follows:

$$F_{ai\_new} = F_{ai} + \mu\left(F_{ri} - F_{ai}\right) \tag{3}$$

where F_{ai} is the initial iteration force at the current time step, F_{r1} is the reaction force calculated at the current time step, and μ is the relaxation factor during the iteration process, which ensures the computational efficiency of the correction. In this section, the optimal relaxation factor is selected as 0.35 [16].

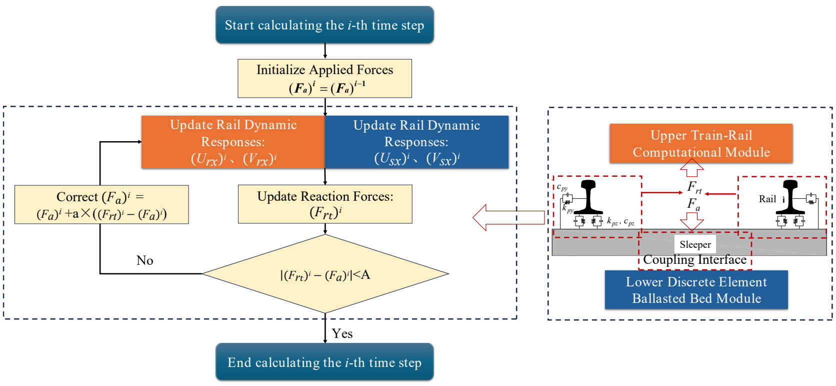

Fig. 3. Flowchart diagram of the coupling process of the rail-fastener-sleeper region.

2.3 Ballast Particle-Mass Block-Spring Damper Coupling Module

Furthermore, coupling is extended between the DEM ballast model and the equivalent mass blocks in the MBD model. Since ballast particles in DEM are discrete, and mass blocks in MBD are interconnected via spring-damper systems, direct coupling is impractical. The DEM ballast assembly was equivalently partitioned into 17 discrete particle groups, and viscoelastic artificial boundaries were introduced on both lateral sides. The spring-damping forces from the MBD model are discretized into equivalent stress acting on the DEM boundary particles. Specifically, the ballast is discretized into 17 equal-mass elements, each with an equivalent mass of 180 kg achieved by particle grouping. And the normal and tangential stresses corresponding to the discretized spring-damper forces can be expressed [18]:

$$F^p = \begin{Bmatrix} F_n \\ F_s \end{Bmatrix} = -D_b^2 [\begin{matrix} \beta_{3p} C_n & 0 \\ 0 & \beta_{3s} C_s \end{matrix}] \begin{Bmatrix} \dot{u}_n \\ \dot{u}_s \end{Bmatrix} - D_b^2 [\begin{matrix} K_n & 0 \\ 0 & K_s \end{matrix}] \begin{Bmatrix} u_n \\ u_s \end{Bmatrix} \quad (4)$$

where F_n and F_s are the normal and tangential forces applied to the boundary particles, respectively; and β_{3p} and β_{3s} are dimensionless correction coefficients, respectively. These coefficients significantly influence wave transmission efficiency. Upon calibration, the optimized values are β_{3p}=1.14 and β_{3s}=1.18.

For the longitudinal coupling module in the ballast between the MBD model and DEM model, the detailed computational procedure is illustrated in Fig. 4. At each time step i, the initial interaction force is derived from the spring-damper forces acting between adjacent ballast mass blocks at time step i-1. Subsequently, Eq. (4) is utilized to compute the equivalent discrete force which is applied to the lateral boundaries of the model in the DEM model. Next, the DEM and MBD modules are solved synchronously to update the dynamic response of the system. During this process, particle boundary-crossing events are checked and, if present, trigger a regrouping of particles to maintain correct periodicity. If no boundary crossing occurs, the centroid response of the 17 ballast mass units is transferred to the MBD system to compute the spring-damper force for the next timestep.

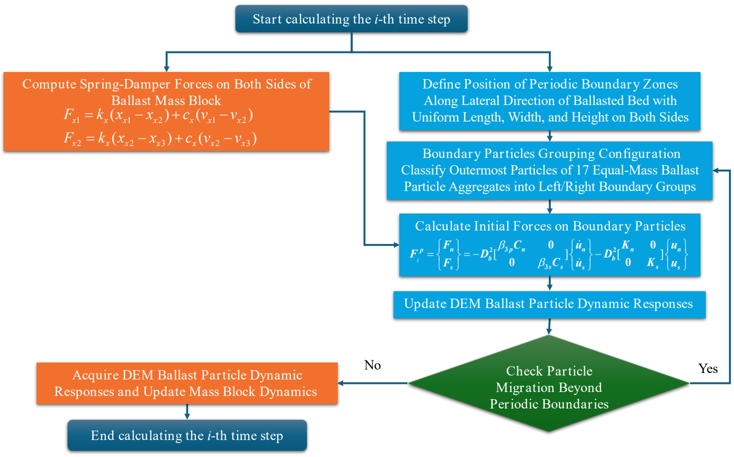

Fig. 4. Flowchart diagram of the coupling process between ballast particles and mass blocks.

2.4 Numerical Model Validation

To validate the accuracy of the proposed coupled modeling framework, calibration was performed at a speed of 295 km/h. As illustrated in Fig. 5, the simulation results were compared against field measurement data [19] and Train-track-roadbed coupling model (MBD-FEM) result [20]. It should be noted that the acceleration curve were filtered prior to comparison in order to facilitate a more reliable evaluation of the results.The predicted vertical acceleration of the rail from the 3D coupled model shows high consistency with the field data, particularly in waveform characteristics. It should be noted that the comparative results indicate that the incorporation of the DEM used to simulate ballast particles, significantly enhanced the model's capability to capture the vertical rebound characteristics of the rail. Specifically, the proposed model successfully predicts positive vertical displacements of the rail, indicating that the rail exhibits upward vertical motion consistent with experimental observations, an effect that reference models fail to accurately reproduce. In summary, the research findings conclusively demonstrate that the 3D MBD-DEM-FDM coupled model developed in this study is capable of accurately and reliably capturing the dynamic response characteristics of high-speed railway track structures.

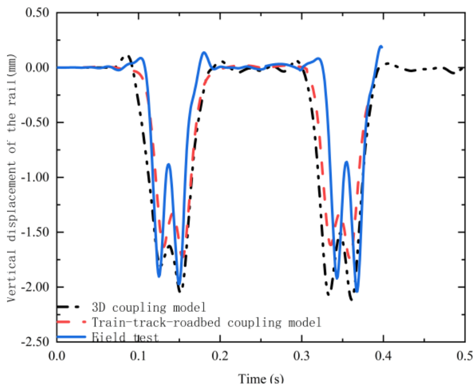

(a) Vertical displacement of rail

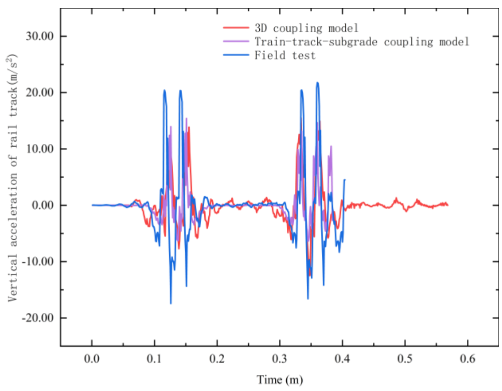

(b) Vertical acceleration of rail

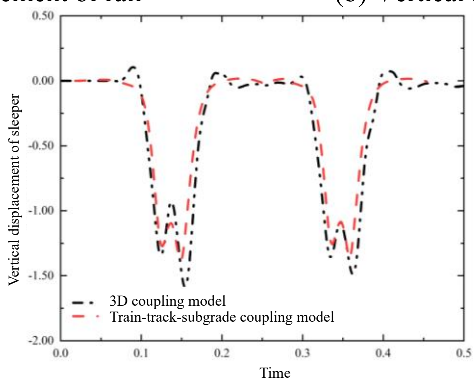

(c) Vertical displacement of sleeper

Fig. 5. Comparison of statistical extremes of structural dynamic responses.

3 Results and discussion

3.1 Macroscopic Dynamic Wheel-Rail Contact Force Responses

Fig. 6 shows the distance-history curves of the vertical wheel-rail contact force for the first wheelset on the left rail at different train speeds. Distance is used as the horizontal coordinate to facilitate direct comparison at identical track locations, since the same travel distance corresponds to different time durations at different speeds. Although the nominal wheel load remains nearly constant at about 80 kN, the dynamic fluctuation of the contact force becomes increasingly significant with increasing speed. As shown in Fig. 7, the average upper peak rises from 88.1 to 95.4 kN, whereas the average lower peak decreases from 72.4 to 63.4 kN. The most evident change occurs between 300 and 325 km/h, indicating a marked intensification of wheel-rail vibration interaction. In addition, the peak locations gradually shift with speed, suggesting that higher speeds alter the spatial distribution of the vehicle–track dynamic interaction. This is mainly attributed to stronger high-frequency excitation and more pronounced inertial and wave-propagation effects in the rail-fastener-sleeper system, which further modify the magnitude and distribution of the wheel-rail contact force. According to the relevant specification [21], the wheel load reduction ratio is calculated from the minimum vertical wheel-rail force, as given in Eq. (9). Fig. 8 presents its fitted relationship with train speed, showing an accelerated increasing trend. Based on the code limit that the wheel load reduction ratio of a continuous force-measuring wheelset should be less than 0.65, the allowable operating speed is estimated to be about 421.7 km/h. Fig. 9 further shows the fitted relationship between the peak lateral contact force of the first wheelset and train speed. The results indicate an exponential increase with speed: below 300 km/h, the increase is relatively moderate, whereas it becomes much more pronounced at 325 km/h and above. This trend is consistent with that of the lateral acceleration response. Moreover, according to the derailment safety criterion [23], the lateral-to-vertical force ratio must remain below 0.8. This requirement is satisfied under all evaluated speed conditions, indicating adequate operational safety margins.

$$\beta = (\bar{P} - P) / \bar{P} \tag{9}$$

where $\bar{P}$, P are the average static wheel weight and the vertical force of the wheel rail, respectively.

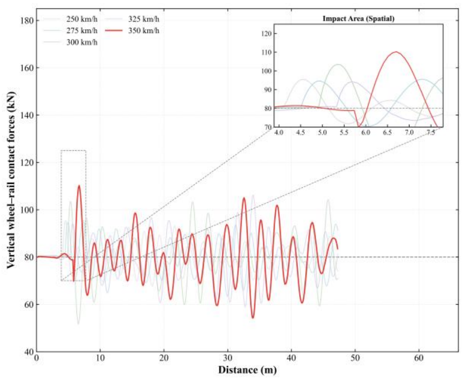

Fig. 6. Distance-history curves of vertical wheel–rail contact forces.

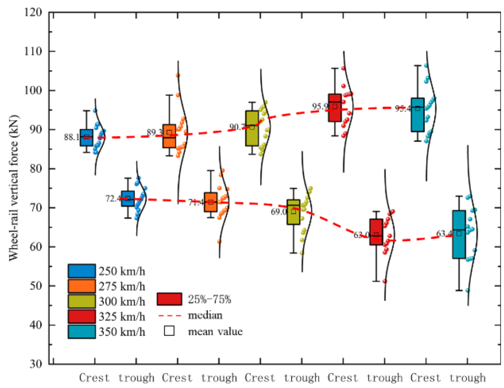

Fig. 7. Box plots of peak vertical wheel-rail contact forces.

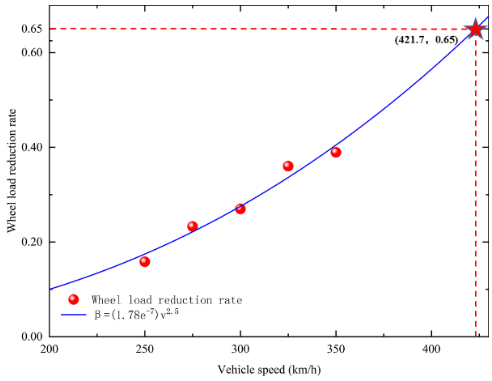

Fig. 8. Fitted curve of wheel load reduction ratio vs. train speed.

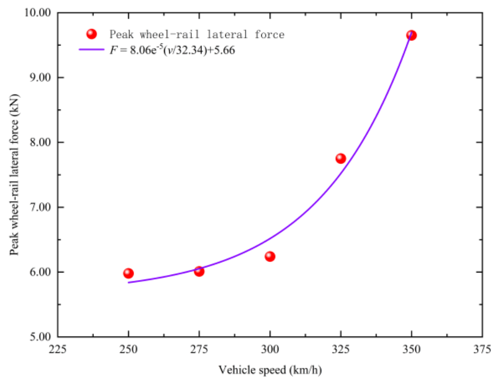

Fig. 9. Fitted curve of peak lateral wheel–rail contact force vs. train speed.

3.2 Macroscopic Dynamic Responses of Rail and Sleeper

For the rail–sleeper macroscopic response, Fig. 10 shows that rail vertical displacement varies significantly with train speed. As speed increases, both the displacement amplitude and waveform change noticeably, with more evident initial rebound and negative displacement at loading onset, indicating a stronger transient unloading effect under high-speed conditions. Meanwhile, the peak displacement occurs progressively later. To quantify this trend, the peak rail displacements at different speeds were extracted and compared with those of the reference model, as shown in Fig. 11(a). The proposed model exhibits a nearly twofold increase in displacement growth rate at 350 km/h compared with the other speeds, revealing a clear nonlinear amplification effect. Although both models show increasing displacement with speed, the proposed model consistently predicts smaller values, especially at lower speeds, likely because the DEM-based ballast representation better captures particle interlocking and thus provides greater structural resistance. A similar trend is observed for sleeper displacement in Fig. 11(b). Fig. 12(a) shows that rail vertical acceleration also increases with speed, while a lagging response appears at the same observation location. As summarized in Fig. 12(b), the proposed model gives lower acceleration peaks than the reference model, with the largest reduction occurring at 250 km/h. However, over the investigated speed range, the peak acceleration in the proposed model increases by 122.4%, compared with 73.2% in the reference model, indicating higher sensitivity to speed-dependent dynamic effects and a stronger capability to capture the influence of ballast granular resistance and energy dissipation.

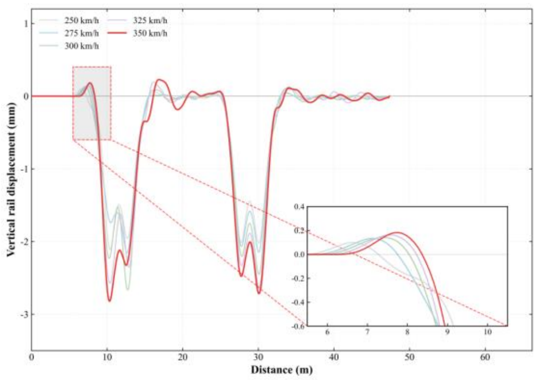

Fig. 10. Distance-history curves of vertical rail displacement.

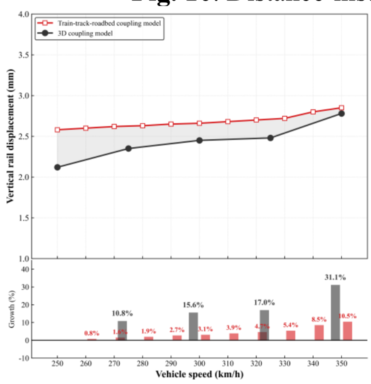

(a) Rail

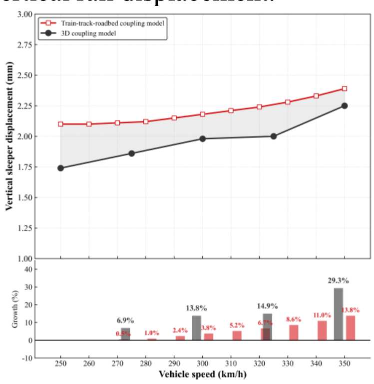

(b) Sleeper

Fig. 11. Variation of vertical peak displacements with train speed.

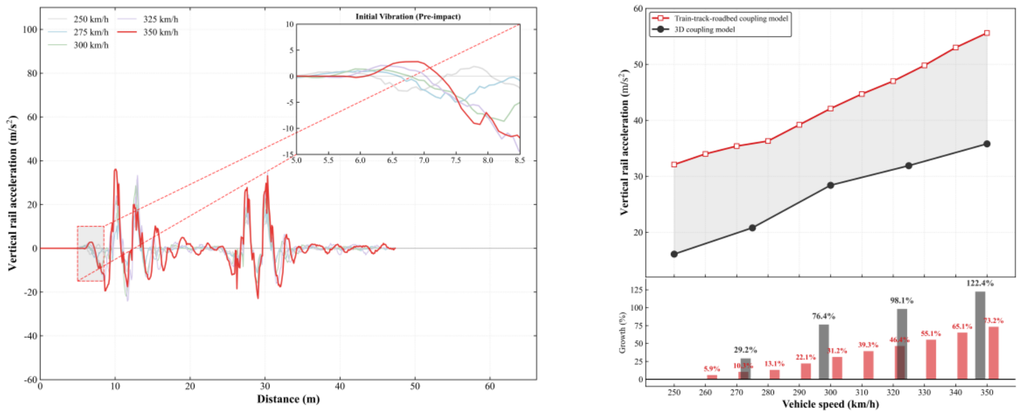

(a) Distance-history curves (b) Peak acceleration vs. Speed

Fig. 12. Variation of vertical rail acceleration with train speed.

3.3 Distribution of Ballast Particle Velocity Fields

To investigate the micromechanical behavior of ballast under high-speed train loading, the particle velocity field within the coupled domain at 300 km/h is shown in Fig. 13, where the black box denotes the coupling region at Sleeper No. 10, and #1 and #2 indicate the first and second wheelsets, respectively. When the first wheelset approaches Sleeper No. 7, ballast particles exhibit the highest velocities and a clear forward motion trend, with intense movement mainly concentrated near the sleeper sides and bottom, especially at the sleeper edges, where an outward splashing tendency can be observed. When the wheelset is directly above Sleeper No. 10, particle velocity decreases to a minimum, approaching a quasi-static state, while sleeper displacement reaches its maximum. This is mainly caused by the uplift of the sleeper ends, which induces local suspension and temporarily weakens particle contact. As the wheelset passes, the ballast show an arch-like motion pattern, with high-velocity zones still concentrated near the sleeper sides. In this stage, outer particles move inward, whereas particles adjacent to the sleeper sides move outward. When the two wheelsets are symmetrically located on both sides of Sleeper No. 10, ballast disturbance weakens and the velocity field gradually concentrates beneath the sleeper. Fig. 13(e)~(h) show that the second wheelset produces a similar but stronger disturbance pattern, with generally higher particle velocities, indicating that the ballast undergoes irreversible disturbance after the first loading. To investigate the effect of train speed on ballast particle motion, the average and peak velocities of the particles were extracted when the first wheelset was directly above Sleeper No. 7, as depicted in Fig. 14. Both the mean and maximum velocities of the ballast particles increase markedly with higher train speeds. However, the growth rate of the average velocity exhibits a decelerating trend, while the peak velocity increases at an accelerating rate. The ratio of the peak velocity to the average velocity, which serves as an indicator of energy concentration within the particle system, decreased from 9.12 at 250 km/h to 7.30 at 325 km/h. This suggests that as the velocity increases, the energy dissipation capacity of the ballast is enhanced. Notably, this ratio reverses its trend and rises back to 7.86 at 325 km/h~350 km/h, implying that 325 km/h may represent a critical transition threshold, which is consistent with the observed nonlinear variations in vertical wheel-rail contact forces.

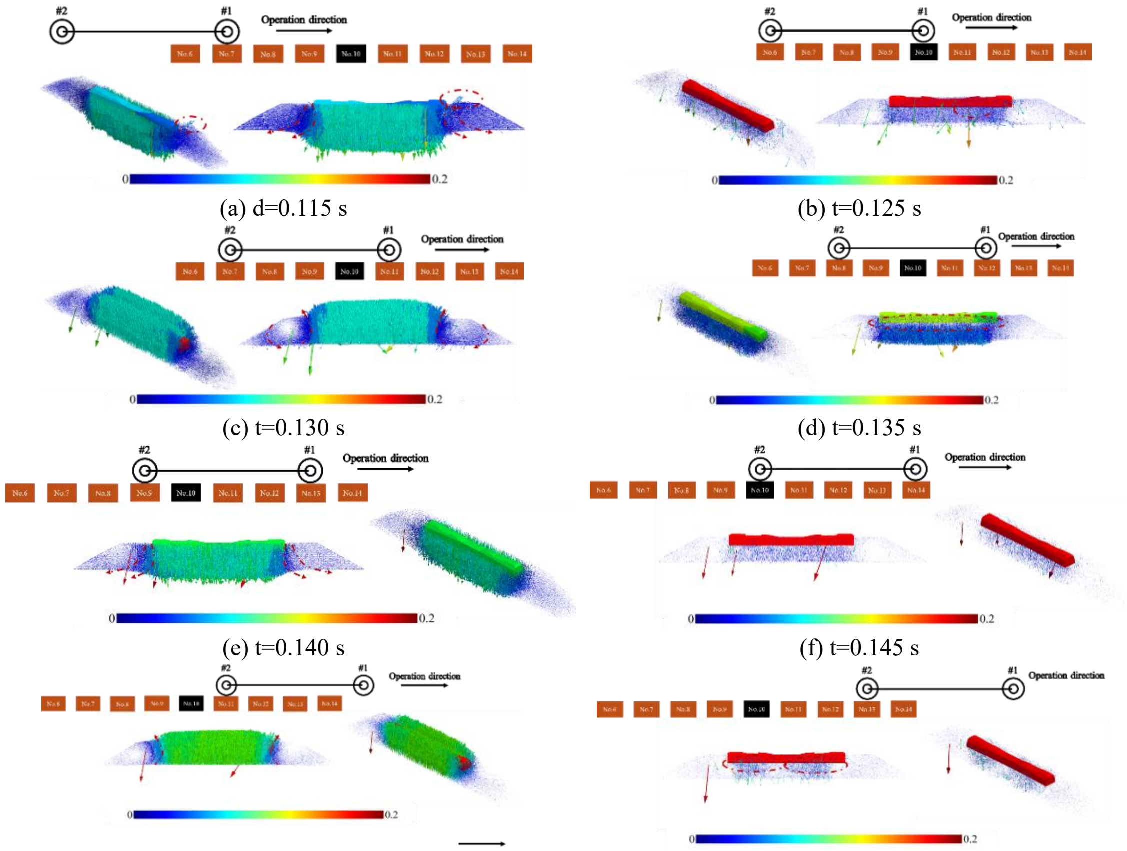

(a) d=0.115 s
(b) t=0.125 s
(c) t=0.130 s
(d) t=0.135 s
(e) t=0.140 s
(f) t=0.145 s
(g) t=0.150 s
(h) t=0.160 s

Fig. 13. Velocity vector field of ballast particles under train loading.

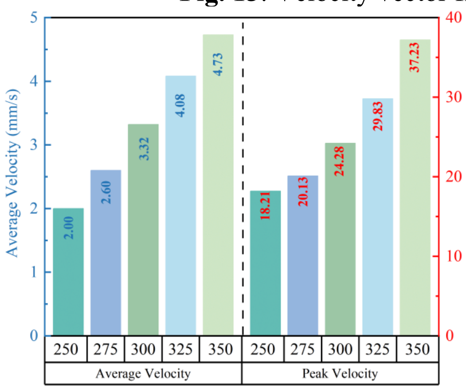

Fig. 14. Statistical analysis results of micromechanical responses

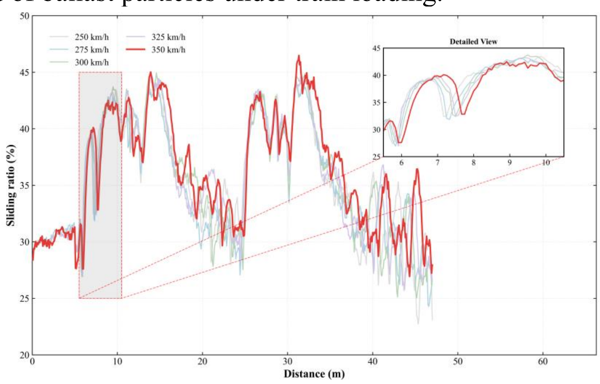

Fig. 15. Temporal variation of internal sliding ratio in the ballast bed.

3.4 Variation in Sliding Ratio

In the DEM model, contact sliding is governed by the Coulomb friction criterion and is assumed to occur when the tangential contact force approaches the critical limit of normal force multiplied by the inter-particle friction coefficient, as defined in Eq. (5). Fig. 15 shows the evolution of the sliding ratio at different train speeds. Because sleeper laying and tamping had been completed before dynamic loading, a certain amount of sliding contact already existed in the initial state. After train loading begins, the sliding ratio rises rapidly to its first peak with an evident lagging feature. The peak appears before the wheelset reaches the sleeper center, indicating that the strongest ballast disturbance occurs slightly ahead of the direct load position, consistent with the forward motion observed in the particle velocity field. In addition, the peak sliding ratio increases with train speed, with increments of about 55%–58% from 250 to 325 km/h and 64% from 325 to 350 km/h, reflecting intensified degradation of particle interlock at higher speeds. After train passage, the sliding ratio gradually returns close to its initial level, indicating a certain recovery capability of the ballast bed.

$$|f_t| / \mu f_n > 0.9999 \tag{5}$$

where f_t and f_n represent the tangential and normal contact forces, respectively, and μ is the inter-particle friction coefficient.

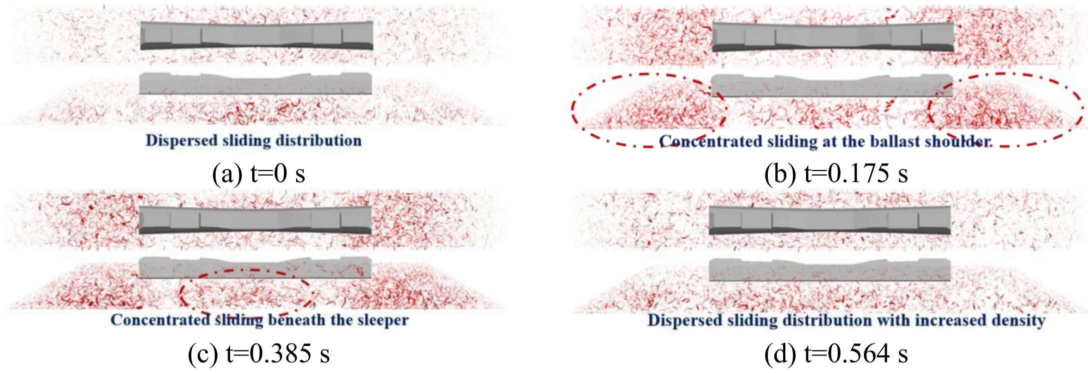

Fig. 16. Contour maps of sliding contact distributions at different time periods.

To further illustrate the spatial distribution of sliding, sliding contact points at different moments were extracted, as shown in Fig. 16. Before train loading, sliding contacts were sparse and mainly concentrated beneath the sleepers, where the normal contact force is relatively small. When the second wheelset passes the sleeper region, the sliding ratio reaches its maximum, and sliding contacts are mainly distributed in the ballast shoulder, while activity beneath the sleeper remains comparatively weak. This suggests a pronounced ratcheting effect, in which particles beneath the sleeper are dominated by vertical compression, whereas lateral slip is more likely to occur in the shoulder zone. As subsequent wheelsets pass, the sliding region expands gradually beneath the sleeper, indicating that the previously compacted ballast structure is progressively disturbed by repeated loading. After the train fully passes, the sliding-contact distribution differs markedly from the initial state, with dense sliding clusters around both the sleeper and shoulder regions. These results suggest that ballast shoulders and sleeper-adjacent zones should be given priority in maintenance and tamping operations.

4 Conclusions

The hybrid MBD-DEM-FDM model demonstrates high accuracy in reproducing field-measured rail and sleeper dynamic response, with errors falling within 5%.

The dynamic responses of the coupled train-track system intensify with increasing train speed. Ballast particles exhibited intensified vibrations near sleeper clips and shoulders, while the theoretical critical velocity of the ballasted railway track structure is estimated to be approximately 421.7 km/h.

Micromechanical analysis reveals a structural transition in the ballast when train speed exceeds approximately 325 km/h, characterized by intensified ballast particle motion and progressive degradation of the interparticle contact force chain network.

A threshold speed of 325 km/h is recommended for ballast bed maintenance intervention. Routine field monitoring should prioritize sub-sleeper and shoulder regions, with reinforcement countermeasures necessitated for ballast zones prone to ballast particle sliding in order to maintain structural stability and service life.

Acknowledgements

Supported by China Railway Group Limited (Practical technology 2023-Special-07), the Science Fund for Distinguished Young Scholars of Hunan Province (2024JJ2073), the National Natural Science Foundation of China, and the High-Performance Computing Center of Central South University.

References

[1] Zhong, K., Li, X., Zhou, Z., 2024. High-speed train-induced vibration of bridge–soft soil systems: observation and MTF-based ANSYS simulation. Buildings 14 (8), 2575.

[2] Zhai, W., Han, Z., Chen, Z., Ling, L., Zhu, S., 2019. Train–track–bridge dynamic interaction: a state-of-the-art review. Vehicle System Dynamics 57 (7), 984–1027.

[3] Liu, M., Gu, Q., Guo, W., Zhou, H., Wang, T., Chang, R., 2025. Numerical simulation for real-time hybrid testing of high-speed maglev train-track-bridge systems under complex loads. Structures 73, 108337.

[4] Sun, Y., Ling, L., 2022. An optimal tangential contact model for wheel–rail non-Hertzian contact analysis and its application in railway vehicle dynamics simulation. Vehicle System Dynamics 60, 3240–3268.

[5] Kurhan, D., Fischer, S., Khmelevskyi, V., 2025. Mathematical modeling of the rail track superstructure–subgrade system. Geotechnics 5 (1), 20.

[6] Lu, Y., Xie, X., Ma, H., Xiang, P., 2025. Braking performance and response analysis of trains on bridges under seismic excitation. Applied Sciences 15, 6799.

[7] Chen, C., McDowell, G.R., 2016. An investigation of the dynamic behaviour of track transition zones using discrete element modelling. Proceedings of the Institution of Mechanical Engineers, Part F: Journal of Rail and Rapid Transit 230 (1), 117–128.

[8] Indraratna, B., Qi, Y., Ngo, T.N., Rujikiatkamjorn, C., Neville, T., Ferreira, F.B., Shahkolahi, A., 2019. Use of geogrids and recycled rubber in railroad infrastructure for enhanced performance. Geosciences 9 (1), 30.

[9] Qian, Y., Lee, S.J., Tutumluer, E., Hashash, Y.M., Ghaboussi, J., 2018. Role of initial particle arrangement in ballast mechanical behavior. International Journal of Geomechanics 18 (3), 04017158.
[10] Zhang, Z., Xiao, H., Wang, M., Zhang, M., Wang, J., 2021. Research on dynamic mechanical behavior of ballast bed in windblown sand railway based on dimensional analysis. Construction and Building Materials 287, 123052.
[11] Mao, J.F., Xiao, Y.J., Yu, Z.W., Tutumluer, E., Zhu, Z.H., 2021. Probabilistic model and analysis of coupled train-ballasted track-subgrade system with uncertain structural parameters. Journal of Central South University 28 (7), 2238–2256.
[12] Xiao, Y., Shen, Z., Tan, P., Hua, W., Wang, M., Jitsangiam, P., 2024. Evaluating enhancement effect of bottom groove shape on lateral resistance of frictional sleepers in ballasted railway track via hybrid DEM-FDM approach. Construction and Building Materials 436, 136755.
[13] Li, L., Liu, W., Ma, M., Jing, G., Liu, W., 2019. Research on the dynamic behaviour of the railway ballast assembly subject to the low loading condition based on a tridimensional DEM-FDM coupled approach. Construction and Building Materials 218, 135–149.
[14] Baghban, H., Arulrajah, A., Narsilio, G.A., Horpibulsuk, S., 2021. DEM simulation of the thermo-geomechanical effect of recycled concrete aggregate assemblies in geothermal pavement bases. Transportation Geotechnics 28, 100528.
[15] Itasca Consulting Group Inc., 2004. Particle Flow Code. Software manual. Itasca Consulting Group Inc., Minneapolis.
[16] Liu, Z., Feng, B., Tutumluer, E., 2023. Coupling train–track models with the discrete element method for realistic simulation of ballasted track dynamics. Transportation Research Record 2677, 414–427.
[17] Wilson, E.L., Farhoomand, I., Bathe, K.J., 1973. Nonlinear dynamic analysis of complex structures. Earthquake Engineering and Structural Dynamics 1, 241–252.
[18] Zhang, W., 2016. Study on vibration of subgrade-ballastless track-vehicle coupled system under irregularities condition. PhD thesis. Southwest Jiaotong University.
[19] Luo, Q., Fu, J., Liu, K., Wang, T., Feng, G., 2021. Monitoring of train-induced responses at the asphalt support layer of a high-speed ballasted track. Constr. Build. Mater. 298, 123909.
[20] Chang, Z., 2022. Vibration analysis and engineering applications of a three-dimensional high-speed train–ballasted track–subgrade coupling system. Cent. South Univ.
[21] Kuhlmeyer, R.L., Lysmer, J., 1973. Finite element method accuracy for wave propagation problems. J. Soil Mech. Found. Div. ASCE 99, 421–427.
[22] Fang, C., Gong, J., Jia, M., Nie, Z., Li, B., Mohammed, A., Zhao, L., 2021. DEM simulation of the shear behaviour of breakable granular materials with various angularities. Adv. Powder Technol. 32, 4058–4069.